Universal Modeling Methods of Induction Machines to Study the Influence of Rotor Existence on Terminal Overvoltages During Inverter-Fed Operation

1st Hujun Peng
Institute of Electrical Machines (IEM)
RWTH Aachen University
Aachen, Germany
hujun.peng@iem.rwth-aachen.de

2nd Yue Yu
Institute of Electrical Machines (IEM)
RWTH Aachen University
Aachen, Germany
yue.yu@iem.rwth-aachen.de

3rd Simon Steentjes
Institute of Electrical Machines (IEM)
RWTH Aachen University
Aachen, Germany
simon.steentjes@iem.rwth-aachen.de

***Abstract*—This study introduces a comprehensive approach to evaluating the influence of the rotor in induction machines on motor terminal overvoltages in inverter-fed operations. To facilitate this analysis, precise grey-box models have been developed for induction machines both with and without rotors. The accuracy of these models is validated by impedance spectrum comparisons between simulated and experimental data, demonstrating a maximum relative error of less than 5 % within a frequency range of up to 5 MHz. Subsequently, a system model incorporating these refined induction machine models along with cable models is employed to investigate the overvoltage phenomenon at the motor terminals. The findings indicate that the presence of the rotor has a negligible impact on terminal overvoltages in induction machines.**

***Index Terms*—Electrical machine, Induction motor, High-frequency modeling.**

I. Introduction

WIDE-bandgap (WBG) semiconductors, particularly silicon carbide (SiC), are increasingly utilized in power converters for electric vehicle drive systems. Compared to traditional silicon-based IGBTs, SiC-based power converters provide notable benefits, including higher switching frequencies, reduced switching losses, and enhanced tolerance to elevated voltages and temperatures [1]. However, despite these advantages, WBG semiconductors also introduce certain challenges, primarily stemming from their rapid switching speeds and high voltage slew rates. The increased switching frequency significantly amplifies common-mode currents and conducted electromagnetic emissions. This effect arises from the parasitic capacitance between motor windings and the stator housing, which becomes increasingly influential at higher frequencies [2]. Another critical issue is the elevated voltage slew rate, which exacerbates voltage stress on the motor insulation system due to the phenomenon of voltage reflection [3]. Additionally, under high dv/dt conditions, the voltage distribution across coil windings in electric machines becomes increasingly uneven [4], raising the likelihood of partial discharge occurrences. To ensure the long-term reliability of low-voltage electric motors operating below 700 V, compliance with IEC 60034-18-41 mandates that partial discharges must be effectively mitigated throughout their operational lifespan [5].

The characteristics of overvoltages at motor terminals, including their magnitude and oscillation frequency, are influenced by multiple factors. These include the impedance spectrum of the motor, the properties of the interconnecting cable between the motor and inverter, and the effectiveness of any filtering mechanisms implemented to limit voltage slew rates [6]. Consequently, a well-coordinated design of these components is essential to mitigate peak voltage levels in inverter-fed drive systems. To achieve an optimal balance between performance and reliability, a comprehensive design approach must take into account multiple interdependent parameters within the electrical drive system [7]. This necessitates the development of accurate high-frequency models for electrical machines to facilitate precise analysis and optimization.

High-frequency modeling of electrical machines can generally be classified into two main approaches: white-box models and grey-box models. White-box modeling involves parameterizing an equivalent electrical circuit based on Finite Element Analysis (FEA) [8]. To accurately represent frequency-dependent mutual impedance effects between adjacent conductors, transmission-line modeling is typically utilized [9]. Although this method offers a high level of detail and accuracy, its primary drawback lies in the significant computational resources required for implementation.

In contrast, grey-box modeling focuses on external interactions of electrical machines without explicitly resolving the voltage distribution along the windings [10]. This approach employs lumped-parameter representations, with parameter estimation achieved through optimization algorithms. Grey-box models have been extensively developed for both induction machines and surface-mounted permanent magnet synchronous motors (PMSMs) [11]. For PMSMs, specifically surface-mounted configurations, these models have been validated for frequencies reaching up to 10 MHz [12], [13]. However, a key limitation of this approach is its omission of mutual impedance effects between phases. Additionally, the absence of a strong physical foundation in model construction restricts its generalization to other machine types and operating conditions.

The lack of a universally applicable grey-box model that can accommodate different motor types presents a notable gap in existing research. Addressing this limitation, the present study introduces the following key contributions:

- Development of grey-box models for induction machines, formulated based on the number of resonance points observed in measured impedance spectra.
- Investigation of the impact of rotor presence on voltage oscillation peak values at motor terminals in inverter-fed operations, conducted through simulation-based analysis.

The structure of this paper is as follows: Section II introduces the high-frequency modeling approach for induction machines, which is derived from impedance spectrum measurements. Next, Section III investigates the influence of rotor presence on motor terminal overvoltages in inverter-fed operations. Finally, Section IV presents the conclusions and outlines future research directions.

II. High-frequency modeling based on impedance measurement

The induction machine examined in this study features two pole pairs and 36 slots. It is mounted on a dedicated testing platform, as shown in Fig. 1. A distinguishing characteristic of this setup is the detachable rotor of the induction motor, illustrated in Fig. 1b. To minimize potential interference from the metallic test bench, an insulating layer is strategically placed between the motor housing and the testing platform, as demonstrated in Fig. 1a.

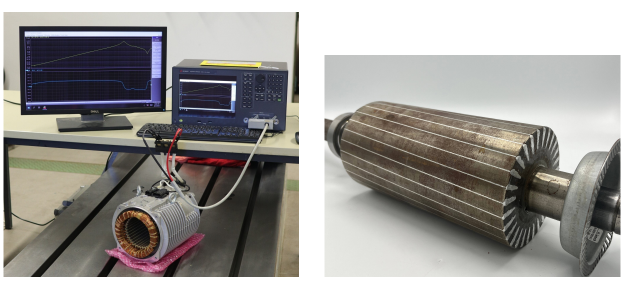

(a) (b)

Fig. 1. Induction machine to be measured: (a) Without rotor, (b) Rotor of the induction machine.

Impedance spectra are measured at the motor terminals under different configurations, including phase-to-housing, phase-to-phase, and phase-to-two-phases, as detailed in Table I. The phase-to-housing configuration represents the common-mode impedance, whereas the phase-to-phase and phase-to-two-phases configurations correspond to differential-mode impedance. Common-mode modeling of electrical machines is essential for evaluating conductor-to-housing voltage, bearing voltage, and slot insulation design. In contrast, differential-mode modeling is crucial for determining maximum phase-to-phase voltage, which directly influences phase-to-phase and conductor-to-conductor insulation requirements. The choice of these impedance measurement topologies is based on their practical accessibility, allowing engineers to perform high-frequency modeling without requiring significant modifications to the electrical machines. The impedance spectra are acquired using a Keysight E4990A impedance analyzer, covering a frequency range from 100 Hz to 10 MHz. This instrument records the amplitude and phase response across various frequencies for different motor terminal connections, as specified in Table I. In these configurations, "UV" indicates a short-circuit connection between terminals U and V, while "GND" denotes a direct link to the motor housing.

TABLE I
Terminal connection configurations for impedance spectrum measurement of the induction motor.

Symbol	Meaning
U-GND	Impedance spectrum measurement between U and GND
V-GND	Impedance spectrum measurement between V and GND
W-GND	Impedance spectrum measurement between W and GND
U-V	Impedance spectrum measurement between U and V
V-W	Impedance spectrum measurement between V and W
W-U	Impedance spectrum measurement between W and U
U-VW	Impedance spectrum measurement between U and VW
V-WU	Impedance spectrum measurement between V and WU
W-UV	Impedance spectrum measurement between W and UV

Impedance measurements are performed separately for the induction machine in configurations with and without the rotor. The impedance spectra for the rotorless induction machine are illustrated in Fig. 2, with the phase-to-ground response depicted in Fig. 2a and the phase-to-two-phases configuration shown in Fig. 2b. Due to the inherent symmetry of the induction motor without a rotor, minimal variation is observed among the impedance characteristics of the three phases. Similarly, the impedance spectra for the induction machine with the rotor are presented in Fig. 3. The close resemblance of impedance profiles across different phases highlights the high degree of symmetry in the motor when the rotor is installed. To analyze the rotor's effect on impedance characteristics, a comparative evaluation is provided in Fig. 4. A key observation is the increased amplitude of differential-mode impedance in the motor with the rotor compared to the rotorless configuration, as shown in Fig. 4a and Fig. 4b. This difference is attributed to the rotor's presence, which reduces the air gap and consequently raises the low-frequency differential impedance.

Additionally, in the phase-to-two-phases configuration (illustrated in Fig. 4b), three distinct resonance points are observed within the impedance spectra, extending up to 5 MHz. These resonance points play a crucial role in the modeling process. The following sections will introduce a scalable grey-box model designed to accurately capture all key resonance points identified in the impedance spectra. Notably, this modeling approach offers flexibility and can be adapted to various types of electrical machines. The number of branches

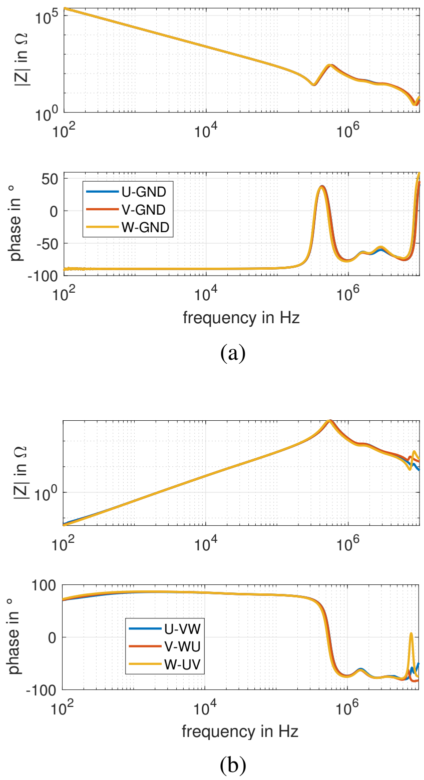

Fig. 2. Impedance spectra for different terminal configurations of the induction machine without a rotor: (a) phase-to-housing, (b) phase-to-two-phases.

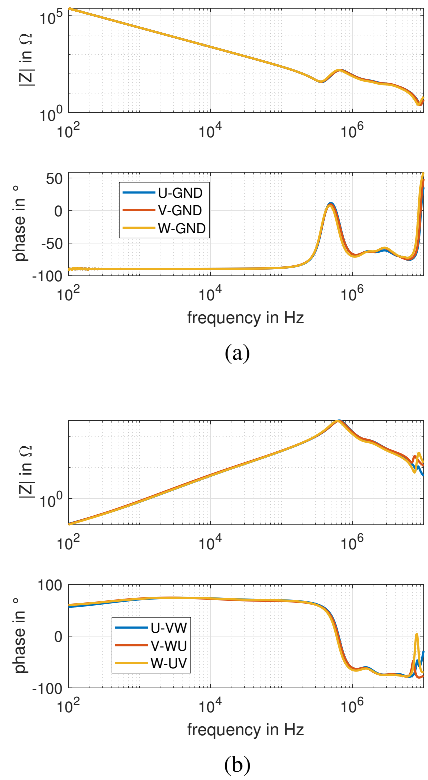

Fig. 3. mpedance spectra for different terminal configurations of the induction machine with a rotor: (a) phase-to-housing, (b) phase-to-two-phases.

within the model can be systematically adjusted to correspond with the primary resonance points detected in the impedance spectrum, ensuring its applicability across different machine configurations.

The proposed grey-box model for the induction machine accounts for the interaction between capacitances and inductances, resulting in three primary resonance points within the impedance spectrum. To effectively capture these resonance characteristics, the model employs an equivalent electrical circuit comprising two branches, labeled as ”1” and ”2,” as illustrated in Fig. 5. Each branch corresponds to a distinct set of resonance points and represents different sections of the phase winding.

Branch 2 models the portion of the phase winding situated near the neutral point, whereas Branch 1 represents the outermost section, closer to the motor terminal. To illustrate the working principles of the grey-box model, phase U is analyzed as an example, demonstrating how three resonance points emerge in the impedance spectrum. The inductive elements in Branch 2 are implemented using an ”RL”-ladder network to account for the skin effect at higher frequencies. The capacitive elements are divided into two components: one modeling the capacitance between the winding and housing, and the other representing the capacitance between windings. Additionally, a resistance is included to account for the insulation layer's resistance along the common-mode path between the windings and housing.

At low frequencies, the capacitive elements in the equivalent circuit have a negligible influence, leaving the impedance primarily dictated by the ”RL”-ladder network. As frequency increases, this results in a rising impedance magnitude, as depicted in Fig. 4b. However, with further frequency escalation, the capacitive elements in Branch 2 start to dominate, effectively short-circuiting the corresponding inductive components. This transition leads to the first resonance point, marked by a noticeable drop in impedance. The second resonance point arises due to the interaction between the inductive component in Branch 1 and the capacitive component in Branch 2, causing an increase in impedance magnitude. Similarly, for the third resonance point, the capacitive effect within Branch 1 becomes dominant, leading to another decline in impedance amplitude.

To enhance modeling accuracy within the mid-frequency range, where most resonance points occur, the inductive component in Branch 1 is refined with three ”RL”-layers. The electrical circuit depicted in Fig. 5 incorporates various parameters, including minor inductances and resistances associated with external supply lines (e.g., L_{00} and R_{00}), as well as impedance elements ($R_{\mathrm{sf},i,j}$ and $C_{\mathrm{sf},i,j}$) representing the interaction between the stator winding and housing in each branch.

To ensure consistency across different phases, the parameter

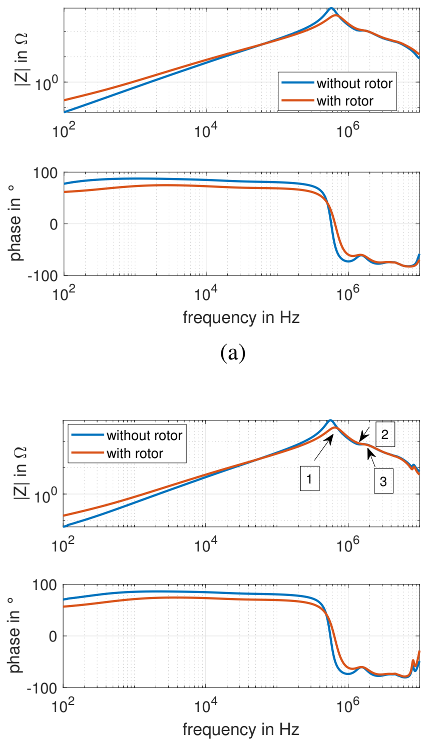

Fig. 4. Comparison of impedance spectra for the induction machine with and without a rotor: (a) phase-to-phase, (b) phase-to-two-phases.

values in Branches 1 and 2 are kept within a relatively small range, as impedance spectra typically exhibit minimal variation among phases in induction machines. A distinguishing feature of this model is the incorporation of frequency-dependent mutual inductances (T1–T2), setting it apart from existing state-of-the-art models. The grey-box model, which consists of 57 parameters, is optimized using the differential evolution algorithm described in [14], minimizing the relative error between the modeled and measured impedance spectra.

To validate the high-frequency domain modeling of the induction machine, the modeled impedance spectra are compared against experimentally measured spectra across multiple terminal configurations. These configurations include phase-to-housing, phase-to-phase, and phase-to-two-phase impedance measurements. To quantify the deviation between the modeled and measured impedance at a specific frequency f_i, an index $\Delta(f_i)$ is introduced, as defined in Eq. (1). This metric represents the relative error between the modeled and measured impedance values at each frequency point. Further, the average deviation Δ_{avg} is computed using Eq. (2), providing an overall measure of how closely the modeled impedance spectrum aligns with the experimental data. To assess the model's performance across different measurement topologies, the parameter $\overline{\Delta}_{\mathrm{mean}}$ is introduced in Eq. (3). This parameter represents the mean deviation Δ_{avg} across all measurement configurations, where N denotes the total number of impedance measurement topologies.

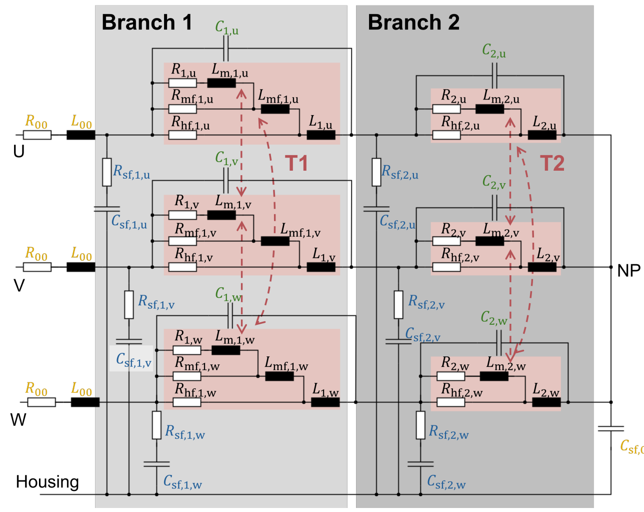

Fig. 5. Grey-box model of the induction machine incorporating two mutual inductances (T1–T2) among phases, represented by dashed lines.

$$\Delta(f_i) = \left| \frac{|Z_{\mathrm{model}}(f_i)| - |Z_{\mathrm{meas}}(f_i)|}{|Z_{\mathrm{meas}}(f_i)|} \right| \quad (1)$$

$$\Delta_{\mathrm{avg}} = \frac{\sum_{i=1}^{\mathrm{n}} \Delta(f_i)}{n} \quad (2)$$

$$\overline{\Delta}_{\mathrm{mean}} = \frac{\sum_{i=1}^{N} \Delta_{\mathrm{avg}}(i-\mathrm{th\ topology})}{N} \quad (3)$$

As illustrated in Fig. 6, the average relative deviations between the modeled and measured impedance spectra are presented across the frequency range of 1 kHz to 5 MHz for both configurations: the induction machine with and without a rotor. Notably, the mean relative deviation remains consistently below 5 %, demonstrating the accuracy of the proposed modeling approach.

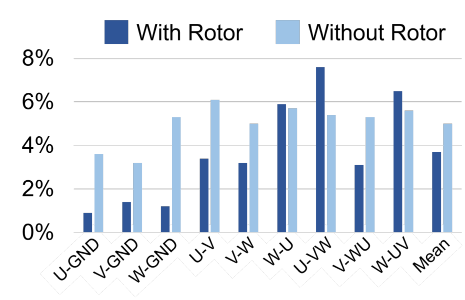

Fig. 6. Relative deviations between the modeled and measured impedance spectra for the induction machine in configurations with and without a rotor.

A detailed comparison between the modeled and measured impedance spectra of the induction machine is provided in Fig. 7 for the rotorless configuration and Fig. 8 for the configuration with a rotor. Specifically, Fig. 7 illustrates the modeling results in the absence of a rotor, whereas Fig. 8 presents the corresponding results when the rotor is included. A key observation from this analysis is the strong agreement between the modeled and measured impedance values across various motor terminal configurations, encompassing both common-mode and differential-mode spectra, for frequencies up to 1 MHz. This consistency highlights the effectiveness and robustness of the proposed high-frequency modeling approach in accurately representing the motor's behavior, regardless of rotor presence. In the following section, a grey-box model for power cables is introduced. By virtually coupling the induction motor to this cable model, simulations are conducted to investigate the influence of the rotor on motor terminal voltages.

III. Influence of the Rotor Existence on Voltage Oscillation Behaviors on Induction Motor Terminals

Since the induction motor under study features a detachable rotor, it is non-operational, preventing direct testing on a physical test bench. Consequently, the analysis of how rotor presence or absence affects motor terminal voltages must rely on simulation-based investigations. To enhance the practical relevance of these simulations, the voltage signals used as input for estimating motor terminal voltages are sourced from an actual test bench. This test setup consists of an IGBT-based inverter, connecting cables, and a commercially available PMSM from an electric vehicle. The schematic representation of this experimental setup is illustrated in Fig. 9, where an extended cable facilitates the connection between the inverter and the PMSM within the laboratory environment.

A physical view of the test bench is provided in Fig. 10, showcasing the setup equipped with four differential voltage probes and an oscilloscope. During PMSM operation, the oscilloscope records three voltage signals at the inverter output—measuring both phase-to-phase and phase-to-ground voltages. These recorded voltage signals serve as inputs for a virtual system, comprising a cable model from [15] and the induction motor models introduced in Section II. Using this virtual system, motor terminal voltages can be computed, with transfer functions playing a crucial role in determining the phase-to-phase voltage at the induction motor terminals. Since the induction motor model exhibits different impedance characteristics depending on rotor presence, the motor terminal voltages are computed for both scenarios—with and without the rotor. This comparative analysis enables a clear assessment of the rotor's influence on motor terminal voltage behavior.

The voltage slew rate of the phase-to-ground voltage at the inverter output is graphically represented in Fig.,11. For the IGBT-based inverter, this parameter is estimated to be approximately 3.3 kV/μs. These voltage signals are recorded under specific operating conditions, including a DC-link voltage of 600 V, a rotational speed of 500 min^{-1}, a switching frequency of 2.5 kHz, and a q-axis current of 5 A. To facilitate further analysis, Fourier series coefficients are computed for each input voltage signal, extending up to the 3000-th harmonic of the 2.5 kHz switching frequency.

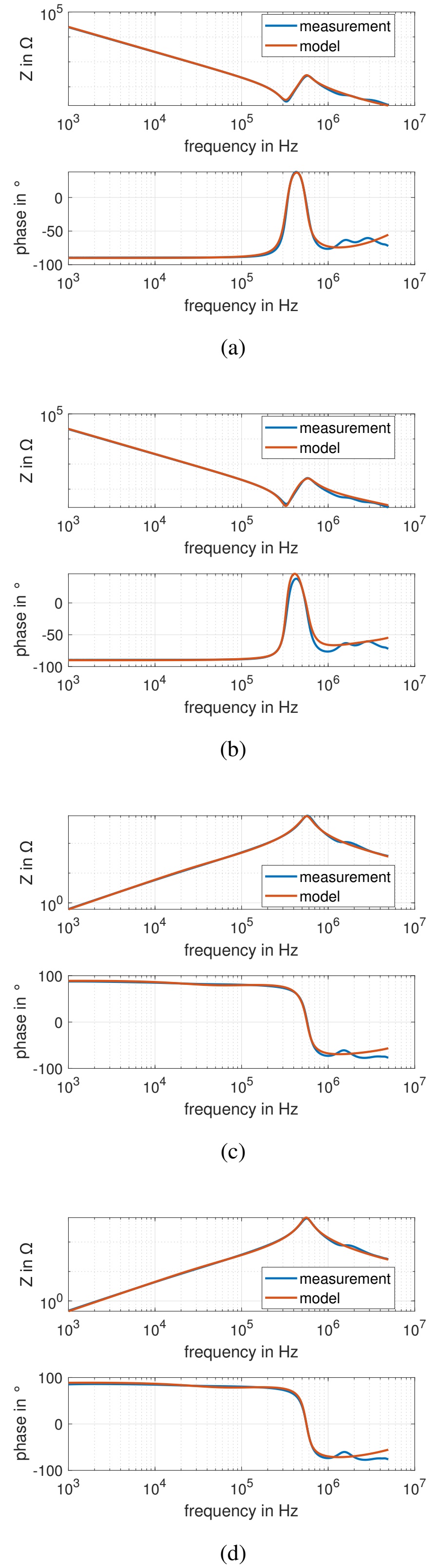

Fig. 7. Evaluation of impedance modeling by comparison with measured values for the induction machine without a rotor: (a) U-GND, (b) V-GND, (c) U-V, (d) U-VW.

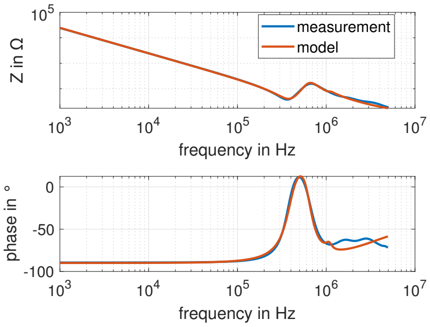

(a)

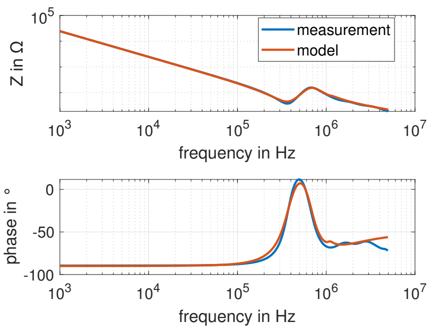

(b)

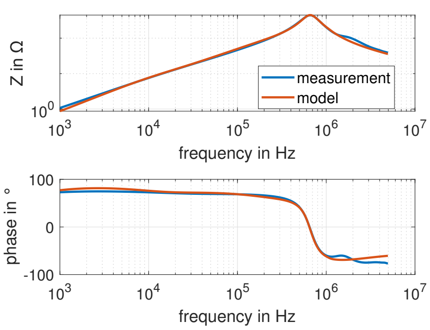

(c)

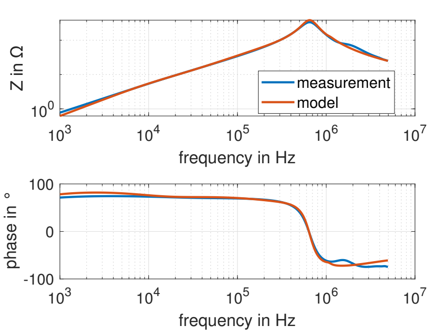

(d)

Fig. 8. Evaluation of impedance modeling by comparison with measured values for the induction machine with a rotor: (a) U-GND, (b) V-GND, (c) U-V, (d) U-VW.

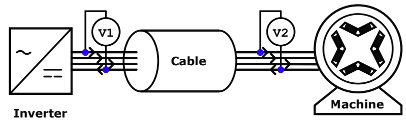

Fig. 9. Schematic of the test bench setup for voltage signal acquisition in the real test environment.

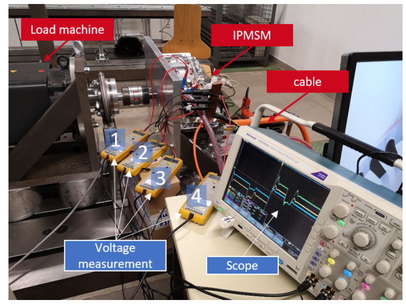

Fig. 10. Test bench configurations for acquiring real voltage signals at the inverter output.

In Fig. 12, the computed phase-to-phase voltage between terminals U and V is presented, derived using the Fourier transform and its inverse, applied to the induction motor model both with and without the rotor. However, a noticeable phase discrepancy is observed in the calculated signals during power module switching. Specifically, the computed signals exhibit an initial drop before rising, whereas the actual signals show a direct increase. This deviation stems from the cost function defined in Eq. (1), which relies solely on amplitude information from the impedance spectra, excluding phase data. To minimize the impact of this phase error, the voltage jump in the calculated signal is interpreted as the peak voltage at the induction motor terminals. This approach is justified by the primary objective of the analysis—to compare the relative difference in simulated voltage peaks between the two motor configurations (with and without the rotor)—rather than focusing on absolute voltage values. The computed voltage spike for the induction motor with a rotor is 947.3 V, closely aligning with the 948.4 V recorded for the rotorless configuration. Moreover, the oscillation frequency during switching remains

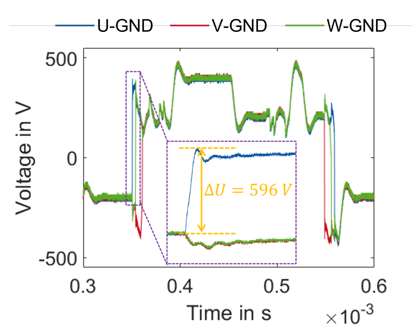

Fig. 11. Recorded phase-to-housing voltage measurements at the inverter output.

virtually identical in both scenarios. Based on these findings, the influence of rotor presence on motor terminal voltages can be considered negligible in the context of inverter-fed operations. One possible explanation is that voltage oscillation behaviors are related to high-frequency behaviors of electrical machines above several 100 kHz, and the flux line will not cross the air gap. As a result, the influence of rotor on the voltage profiles during switching processes can be neglected.

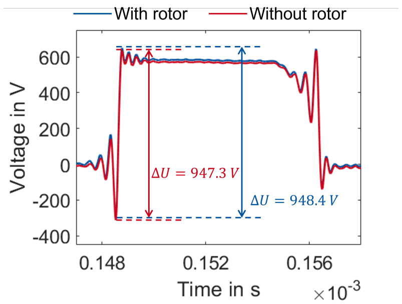

Fig. 12. Comparison of U-V voltage signals for the induction machine with and without a rotor.

IV. Conclusions and Outlooks

This study presents a systematic approach to evaluating the impact of rotor presence in an induction machine on overvoltages at motor terminals. These overvoltages stem from the complex interactions between power converters, cables, and electrical machines. To facilitate this analysis, accurate grey-box models are developed for induction machines, incorporating high-frequency representations for both rotor-present and rotor-absent configurations. Validation against measured impedance spectra demonstrates that these models achieve a remarkably low average relative error of less than 5 %. Building upon this foundation, an integrated system model—comprising both the cable and induction machine—is constructed to compute motor terminal voltages using transfer function principles. The final phase of this study examines how rotor presence influences terminal overvoltages in inverter-fed operations. Simulation results reveal that the impact of rotor presence on overvoltage behavior is minimal, suggesting that high-frequency modeling of induction machines does not require extreme precision when assessing their interactions with inverters and cables. This finding is particularly significant, as it simplifies modeling requirements while maintaining reliability in system-level analyses.

References

[1] A. Bindra, "Wide-bandgap-based power devices: Reshaping the power electronics landscape," *IEEE Power Electronics Magazine*, vol. 2, no. 1, pp. 42–47, 2015.

[2] D. Han, S. Li, Y. Wu, W. Choi, and B. Sarlioglu, "Comparative analysis on conducted cm emi emission of motor drives: Wbg versus si devices," *IEEE Transactions on Industrial Electronics*, vol. 64, no. 10, pp. 8353–8363, 2017.

[3] Y. Jiang, W. Wu, Y. He, H. S.-H. Chung, and F. Blaabjerg, "New passive filter design method for overvoltage suppression and bearing currents mitigation in a long cable based pwm inverter-fed motor drive system," *IEEE Transactions on Power Electronics*, vol. 32, no. 10, pp. 7882–7893, 2017.

[4] J. Dittmann, C.-N. Behrendt, and B. Ponick, "Prediction of the voltage distribution in a inverter-fed hairpin stator winding," in *2022 25th International Conference on Electrical Machines and Systems (ICEMS)*, 2022, pp. 1–6.

[5] R. E. Machines-Part, "Rotating electrical machines-part 18-41: Partial discharge free electrical insulation systems (type i) used in rotating electrical machines fed from voltage converters-qualification and quality control tests," *Geneva, Switzerland: International Electrotechnical Commission*, 2014.

[6] Y. Xie, J. Zhang, F. Leonardi, A. R. Munoz, F. Liang, and M. W. Degner, "Modeling and verification of electrical stress in inverter-driven electric machine windings," in *2018 IEEE Energy Conversion Congress and Exposition (ECCE)*, 2018, pp. 5742–5749.

[7] A. Hoffmann and B. Ponick, "Method for the prediction of the potential distribution in electrical machine windings under pulse voltage stress," *IEEE Transactions on Energy Conversion*, vol. 36, no. 2, pp. 1180–1187, 2021.

[8] X. Ju, Y. Cheng, M. Yang, S. Cui, A. Sun, X. Liu, and M. He, "Voltage stress calculation and measurement for hairpin winding of ev traction machines driven by sic mosfet," *IEEE Transactions on Industrial Electronics*, vol. 69, no. 9, pp. 8803–8814, 2022.

[9] O. Magdun, S. Blatt, and A. Binder, "Calculation of stator winding parameters to predict the voltage distributions in inverter fed ac machines," in *2013 9th IEEE International Symposium on Diagnostics for Electric Machines, Power Electronics and Drives (SDEMPED)*, 2013, pp. 447–453.

[10] K. Vanthuyne, M. Gulec, and P. Sergeant, "High-frequency motor modelling: Parameter variation due to manufacturing," in *2022 International Conference on Electrical Machines (ICEM)*, 2022, pp. 821–826.

[11] M. S. Toulabi, L. Wang, L. Bieber, S. Filizadeh, and J. Jatskevich, "A universal high-frequency induction machine model and characterization method for arbitrary stator winding connections," *IEEE Transactions on Energy Conversion*, vol. 34, no. 3, pp. 1164–1177, 2019.

[12] Y. Wu, H. Li, W. Ma, M. Dong, and Q. Zhong, "High-frequency model of permanent magnet synchronous motor for emi prediction in adjustable speed drive system," in *2018 IEEE International Power Electronics and Application Conference and Exposition (PEAC)*, 2018, pp. 1–6.

[13] Y. Wu, C. Bi, K. Jia, D. Jin, H. Li, W. Yao, and G. Liu, "High-frequency modelling of permanent magnet synchronous motor with star connection," *IET Electric Power Applications*, vol. 12, no. 4, pp. 539–546, 2018.

[14] Y. Zhang, H. Peng, and W. Hofmann, "Transient skin effect in highly dynamic induction motor drives: energy-optimized design," *Electrical Engineering*, vol. 105, no. 2, pp. 1015–1024, 2023.

[15] H. Peng, N. Driendl, S. Stevic, L. Sharifian, Y. Friouz, D. Butterweck, and K. Hameyer, "A study about the influence of rotor position of ipmsm on the maximum voltage on motor terminals under inverter-fed operation," in *2023 IEEE 6th Student Conference on Electric Machines and Systems (SCEMS)*. IEEE, 2023, pp. 1–6.